

# The Observable Thermal and Kinetic Sunyaev-Zel’dovich Effect in Merging Galaxy Clusters

John J. Ruan<sup>1\*</sup>, Thomas R. Quinn<sup>1</sup> and Arif Babul<sup>2</sup>

<sup>1</sup>*Department of Astronomy, University of Washington, Box 351580, Seattle, WA, 98195, USA*

<sup>2</sup>*Department of Physics and Astronomy, University of Victoria, Victoria, BC, V8P 1A1, Canada*

Accepted 2000 December 01. Received 2000 December 01; in original form 2000 October 01

## ABSTRACT

The advent of high-resolution imaging of galaxy clusters using the Sunyaev-Zel’dovich Effect (SZE) provides a unique probe of the astrophysics of the intracluster medium (ICM) out to high redshifts. To investigate the effects of cluster mergers on resolved SZE images, we present a high-resolution cosmological simulation of a  $1.5 \times 10^{15} M_{\odot}$  adiabatic cluster using the TreeSPH code ChaNGa. This massive cluster undergoes a 10:3:1 ratio triple merger accompanied by a dramatic rise in its integrated Compton-Y, peaking at  $z = 0.05$ . By modeling the thermal SZE (tSZ) and kinetic SZE (kSZ) spectral distortions of the Cosmic Microwave Background (CMB) at this redshift with relativistic corrections, we produce various mock images of the cluster at frequencies and resolutions achievable with current high-resolution SZE instruments. The two gravitationally-bound merging subclusters account for 10% and 1% of the main cluster’s integrated Compton-Y, and have extended merger shock features in the background ICM visible in our mock images. We show that along certain projections and at specific frequencies, the kSZ CMB intensity distortion can dominate over the tSZ due to the large line of sight velocities of the subcluster gas and the unique frequency-dependence of these effects. We estimate that a one-velocity assumption in estimation of line of sight velocities of the merging subclusters from the kSZ induces a bias of  $\sim 10\%$ . This velocity bias is small relative to other sources of uncertainty in observations, partially due to helpful bulk motions in the background ICM induced by the merger. Our results show that high-resolution SZE observations, which have recently detected strong kSZ signals in subclusters of merging systems, can robustly probe the dynamical as well as the thermal state of the ICM.

**Key words:** galaxies: clusters: general

## 1 INTRODUCTION

Galaxy clusters are the most massive gravitationally-bound objects in the Universe, and their abundance evolution provides a direct test of the growth of structure. Cluster surveys have provided constraints on cosmological parameters such as  $\Omega_M$ ,  $\Omega_{\Lambda}$ ,  $\sigma_8$ , and  $w_0$  (e.g. Mantz et al. 2008, 2010; Vikhlinin et al. 2009; Rozo et al. 2010; Vanderlinde et al. 2010; Sehgal et al. 2011, for a recent review, see Allen et al. 2011). While cluster research has traditionally relied heavily on X-ray observations, new survey telescopes such as the *Planck* satellite (Planck Collaboration et al. 2011a), the Atacama Cosmology Telescope (ACT, Fowler et al. 2007), and the South Pole Telescope (SPT, Carlstrom et al. 2011) are instead probing the Sunyaev-Zel’dovich Effect (SZE, Zel’dovich & Sunyaev 1969; Sunyaev & Zeldovich 1970, 1972).

Observations of the SZE detect small distortions in the Cosmic Microwave Background (CMB) blackbody spectrum caused by inverse-Compton scattering of CMB photons off energetic electrons in the hot intracluster medium (ICM) (for reviews, see Birkinshaw 1999; Carlstrom, Holder, & Reese 2002). Since this spectral distortion does not suffer from cosmological surface brightness dimming, the SZE has the advantage of being able to detect clusters out to higher redshifts than possible in the X-ray.

Current blind SZE surveys scan large regions of the millimeter and sub-mm sky to detect intensity fluctuations in the CMB from the SZE of individual clusters. These observations have relatively low angular resolutions ( $\gtrsim 1'$ ) and are typically unable to resolve cluster substructures, except in exceptional cases of massive nearby clusters such as the Coma cluster (Planck Collaboration et al. 2012a). Thus, the resulting key observable is the total Compton-Y, integrated over the entire cluster (Equation 1). Using well-known clus-

\* E-mail: jruan@astro.washington.edu

ter scaling relations between various observed quantities such as  $Y$  and the total cluster mass  $M$  (e.g. Arnaud et al. 2010; Marrone et al. 2012; Planck Collaboration et al. 2012b; Sifon et al. 2012; Hoekstra et al. 2012), masses for large samples of clusters can be directly inferred. While the  $Y$ - $M$  scaling relation is tight, there is some intrinsic scatter which may be induced by various phenomena such as cluster mergers and AGN (e.g. Krause et al. 2012; Battaglia et al. 2012, see however Poole et al. 2007). A clear understanding of the sources of intrinsic scatter in cluster scaling relations is crucial, as this scatter will limit the precision of cosmological parameters inferred from SZE surveys.

The advent of high-resolution (10-30'') SZE imaging of clusters opens a new window to the thermal and dynamical state of the ICM. These observations have the ability to resolve small-scale disturbances in the ICM caused by various phenomena, thus probing their effects on the total Compton- $Y$  of each cluster. Bolometer arrays such as the Multiplexed SQUID/TES Array at Ninety GHz (MUSTANG, Dicker et al. 2008) on the Green Bank Telescope (GBT) and Bolocam (Haig et al. 2004) on the Caltech Submillimeter Observatory (CSO), as well as interferometric dish arrays such as the Combined Array for Research in Millimeter-wave Astronomy (CARMA, Bock et al. 2006) and the Atacama Large Millimeter/submillimeter Array (ALMA) are beginning to make these unique observations at a variety of frequencies (Kitayama et al. 2004; Nord et al. 2009; Mason et al. 2010; Korngut et al. 2011; Plagge et al. 2012; Reese et al. 2012; Mroczkowski et al. 2012).

In this paper, we focus specifically on the impact of cluster mergers in high-resolution SZE observations. This is particularly relevant as clusters are assembled through hierarchical growth via mergers in the standard  $\Lambda$ CDM cosmology (Kravtsov & Borgani 2012, and references therein). Since blind SZE cluster surveys will probe high redshifts, a significant fraction of SZE-selected clusters will still be experiencing ongoing mergers. Hydrodynamic simulations of cluster mergers have revealed transient boosts in the total Compton- $Y$  during passages of merging subclusters through the main cluster (Poole et al. 2007; Wik et al. 2008). This can cause SZE surveys to preferentially detect merging systems with overestimated cluster masses, thus biasing the inferred cosmology to higher  $\sigma_8$ , and lower  $\Omega_M$  (Randall, Sarazin, & Ricker 2002; Wik et al. 2008). Indeed, X-ray follow-up of clusters detected by *Planck* have unveiled a new and significant population of disturbed systems (Planck Collaboration et al. 2011b, 2012c). Clusters appearing to be relaxed in X-ray observations have also been found to contain substructures attributed to mergers in high-resolution SZE observations. In the case of RXJ1347.5-1145, substructures in 10'' resolution SZE observations interpreted as a merger shock are estimated to be a 10% effect on observations with 1' resolution (Mason et al. 2010; Korngut et al. 2011).

High-resolution SZE imaging of more clusters will be crucial for understanding the effects of mergers on the integrated Compton- $Y$ , and important for precision cluster cosmology. These observations will require guidance from hydrodynamic cluster simulations to provide a framework for proper interpretation. For example, observed SZE substructures in merging systems are combinations of thermal SZE (tSZ) and kinetic SZE (kSZ) contributions from merger shocks, the remnant cores of merging subclusters, and the

ambient background ICM; simulations are necessary to identify means of disentangle these different effects. Previous studies of the kSZ using cosmological simulations have often focused on the peculiar motions of unresolved individual galaxy clusters as a whole (e.g. Roncarelli et al. 2007), or relatively relaxed (non-merging) clusters (e.g. Diaferio et al. 2005), although Maturi et al. (2007) has investigated the kSZ polarization in merging systems. It is not yet clear how the observable tSZ and kSZ morphology of a cluster will change during a merger, especially at different projections. Our main goal in this paper is to show what a typical merging cluster detected in blind SZE surveys will look like in follow-up high-resolution SZE observations, and how the tSZ and kSZ contribute to the resulting SZE signal. Using a cosmological simulation of a massive cluster undergoing a 10:3:1 triple merger described in Section 2, we model its frequency-dependent tSZ and kSZ distortion on the CMB spectrum. In Section 3, we produce mock SZE intensity maps of the merging cluster at different frequencies and resolutions achievable by current instruments. In Section 4, we discuss the observable SZE substructures from the merger shocks and the kSZ contributions to the observable SZE signal. To separate the sources of the observable SZE signal, we decompose the cluster into its gravitationally-bound components to probe the separate SZE contributions of individual substructures and the background ICM (including the merger shocks). We show that the kSZ can dominate the CMB spectral distortion for merging subclusters at certain projections, and find that multi-frequency SZE-inferred velocities of merging subclusters are biased to only  $\sim 10\%$  from the one-velocity approximation partially due to additional motions in the background ICM induced by the merger. We summarize our results and conclude in Section 5.

Throughout the paper, we adopt a standard  $\Lambda$ CDM cosmology with  $\Omega_M = 0.28$ ,  $\Omega_\Lambda = 0.72$ ,  $\Omega_b = 0.046$ ,  $\sigma_8 = 0.82$ , and  $H_0 = 70 \text{ km s}^{-1} \text{ Mpc}^{-1}$ , consistent with the 5 year *WMAP* results of Komatsu et al. (2009).

## 2 THE SIMULATED CLUSTER

Our cluster was simulated using the cosmological TreeSPH code ChaNGa (Gioachin et al. 2007) and the zoomed-in technique of Katz & White (1993). An initial dark matter (DM) only simulation of a  $400h^{-1} \text{ Mpc}$  periodic cube with  $2.16 \times 10^8$  DM particles of mass  $3.29 \times 10^{10} M_\odot$  was run with initial mass perturbations generated using CMBFAST (Seljak & Zaldarriaga 1996) and the above cosmological parameters. This low-resolution simulation was run to  $z = 0$ , and all resulting cluster haloes were identified using the friends-of-friends algorithm with a linking length of 0.2 times the mean interparticle separation. Formation times were determined for each cluster by determining the epoch at which the most massive progenitor reached 75% of its  $z = 0$  mass. We chose a cluster to resimulate whose formation time was approximately the median of all clusters greater than  $1.5 \times 10^{15} M_\odot$  (note that this mass defined by the friends-of-friends algorithm is slightly different from the virial mass we use below). The initial conditions for the subsequent high-resolution simulation were generated by identifying the Lagrangian region in the lower-resolution simulation that ends up within 3 virial radii of the cho-

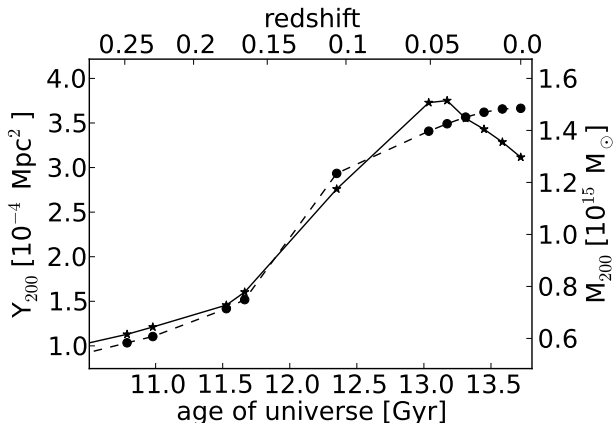


**Figure 1.** The time evolution of the total integrated  $Y_{200}$  (solid) and  $M_{200}$  (dashed) of the main cluster. The epochs sampled by our simulation outputs are also shown. A 10:3:1 triple merger occurring between  $z \sim 0.17$  to  $0.12$  causes a dramatic rise in  $M_{200}$ . There is a corresponding rise in  $Y_{200}$ , although its evolution after the merger deviates from that of  $M_{200}$  as the cluster relaxes.

sen cluster, and resolving this region with DM particles of mass  $5.37 \times 10^7 M_{\odot}$  and gas particles of mass  $1.06 \times 10^7 M_{\odot}$ . This region is surrounded by layers of lower-resolution spherical shells out to the full  $400h^{-1}$  Mpc box. Additional high-resolution perturbations were also applied to particles in the central  $64h^{-1}$  Mpc of this box. These initial conditions for the zoomed-in simulation were then evolved from  $z = 139$  to the present with an ‘adiabatic’ equation of state for the gas. That is, the gas is evolved with no radiative cooling, non-gravitational heating, or star formation, but the gas evolution is not isentropic due to the presence of shocks. Inside the virial radius of this cluster at  $z = 0.05$  (the output at which our SZE analysis is performed), there are only five low-resolution dark matter particles, leading to a total mass of  $\sim 8 \times 10^8 M_{\odot}$  in ‘missing’ gas particles. All the low-resolution DM particles inside the cluster are near the virial radius and are not associated with any subhaloes of the main cluster. This confirms that our simulation analysis is robust to our choice of the size of the zoomed-in region. All analysis and visualization was done using the parallelized simulation visualization tool Salsa<sup>1</sup>, unless otherwise stated.

We identify the cluster centre as the particle at the deepest potential, and determine the properties of the cluster in the spherical volume with an overdensity of  $200\rho_{cr}$  (where  $\rho_{cr}$  is the critical density of the Universe). At  $z = 0$ , the virial radius is  $R_{200} = 2.35$  Mpc, and the total virial mass is  $M_{200,tot} = 1.48 \times 10^{15} M_{\odot}$ . This total mass includes a gas mass of  $M_{200,gas} = 2.22 \times 10^{14} M_{\odot}$  and a DM mass of  $M_{200,DM} = 1.26 \times 10^{15} M_{\odot}$ . Figure 1 shows the evolution of  $M_{200,tot}$  of this cluster over time. The cluster slowly accretes mass from  $z \sim 0.28$  to  $0.17$ , but then undergoes a period of dramatic mass gain due to a triple merger from  $z \sim 0.17$  to  $0.12$ . The mass increase from the triple merger is not sharp in Figure 1 due to the limited time resolution of the outputs. After the mergers, the mass accretion decreases to rates comparable to that from before the merger. By visualizing the simulation at  $z = 0.23$  (before the mergers),

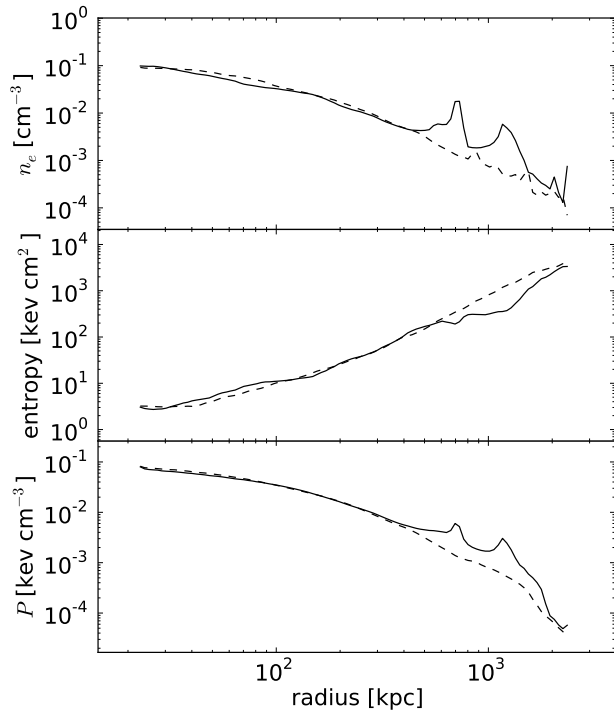


**Figure 2.** Radial profiles of electron number density (top), entropy (middle), and gas pressure (bottom), of the quadrant of the main cluster containing substructures A and B (solid), and the remaining three quadrants for comparison (dashed). The profiles extend out to  $R_{200}$ , and are of the cluster at output  $z = 0.05$ . The effects of the merging substructures A (at 1.14 Mpc) and B (at 0.7 Mpc) are evident. Due to the non-radial trajectories of these merging substructures, the entropy jumps due to their merger shocks are not clearly visible in these radial profiles.

we identify the three pre-merger clusters to determine that the triple merger is approximately 10:3:1 ratio in mass.

The observable tSZ can be parameterized using the total Compton-Y parameter, which is integrated over the full angular extent of the cluster. In our simulation, this is calculated over all gas particles inside  $R_{200}$  of the cluster at each time step using

$$Y_{200} = \int_{V_{200}} n_e \sigma_T \frac{k_B T}{m_e c^2} dV. \quad (1)$$

Due to the relatively low densities and temperatures of the gas outside  $R_{200}$ , the observable SZE signal beyond  $R_{200}$  is negligible. The time evolution of  $Y_{200}$  is also shown in Figure 1. The  $Y_{200}$  increases slowly before  $z \sim 0.17$ , and also experiences a dramatic rise due to the triple merger. As the mass accretion slows down after the merger,  $Y_{200}$  continues to rise from  $z \sim 0.12$  to  $0.05$ , likely due to shocks that form as the merging subclusters travel through the denser interior of the main cluster. Visualization of the cluster at  $z = 0.05$  shows that the merging subclusters in the 10:3:1 merger are in the late stages of their initial pass through the main cluster, with well-developed merger shocks. However, after peaking at  $z \sim 0.05$ , the  $Y_{200}$  then sharply decreases as the cluster begins to relax. Transient boosts in  $Y_{200}$  are also seen in the idealized merger simulations of Poole et al. (2007). The evolutionary tracks of simulated clusters along the Y-M relation during mergers have been investigated in

<sup>1</sup> <http://software.astro.washington.edu/nchilada/>

previous studies (e.g. Poole et al. 2007; Krause et al. 2012), and these deviations are a known source of intrinsic scatter in Y-M scaling relations (but may not be able to account for all of the scatter). While we do not focus on the exact evolution of the Y-M relation in this paper, the peak of the Compton-Y at  $z \sim 0.05$  suggests that the SZE substructures associated with the merger is likely to have the biggest effect on  $Y_{200}$  at this redshift. Furthermore, this peak of the Compton-Y is also when this cluster is most detectable in blind SZE surveys, and so we focus our simulation analysis on this output.

Figure 2 shows radial profiles of the mass-weighted electron number density  $n_e$ , gas entropy  $k_B n_e^{-2/3} T$ , and gas pressure  $P$  at  $z = 0.05$ . We calculate profiles for the quadrant of the cluster containing both merging subclusters, as well as the remaining three quadrants for comparison. The pressure profile for the three quadrants without merging subclusters are in broad agreement with observations of the most massive clusters in Arnaud et al. (2010), as well as the Coma cluster (Planck Collaboration et al. 2012a). At this epoch, the larger merging subcluster in the 10:3:1 triple merger (hereafter substructure A) is 1.14 Mpc from the center of the main cluster, and the cold, dense gas in its remnant core is clearly seen as a jump in the average  $n_e$  and  $P$  at this radius. The strong contrast in  $P$  between substructure A and the background ICM should make substructure A clearly visible in high-resolution SZE images. The smaller merging subcluster in the triple merger (hereafter substructure B) is also visible as a second peak in the  $n_e$  and  $P$  profiles at a radius of 0.70 Mpc. Visualization of this cluster clearly shows merger shocks in front of both substructures A and B in the form of strong temperature increases. However, sharp increases in the entropy profile from the shocks around 0.07 and 1.14 Mpc are not seen in Figure 2 because neither merging substructures have trajectories aligned with the center of the main cluster (i.e., a large component of the velocity vectors of both shocks are in the tangential direction). This purely geometrical effect spreads out the entropy jump from the shock over a large range of radii in Figure 2. In fact, the entropy profile actually decreases around both substructures due to the low entropy of the cold gas in their remnant cores.

### 3 MOCK SUNYAEV-ZEL'DOVICH EFFECT IMAGES

We produce projected tSZ and kSZ maps of the cluster's  $R_{200}$  spherical volume at  $z = 0.05$  by binning the field of view of  $R_{200} \times R_{200}$  along two orthogonal projections into  $100 \times 100$  pixels, each 47 kpc  $\times$  47 kpc physically. Projection 1 was selected such that the line of sight velocities of the merging subclusters in the cluster rest-frame are maximal, while projection 2 is in the perpendicular direction. We expect any interesting effects from the kSZ to be strongest in projection 1, and weakest in projection 2. However, the strong transverse velocities of the substructure gas in the second projection allows us to study the large-scale effects of the merger shocks on the main cluster's ICM. Figure 3 shows projected maps of the cluster's tSZ Compton-y (left panels), mass-weighted over all gas particles inside the cluster virial radius in each pixel, and calculated using

$$y_{tSZ} = \int n_e \sigma_T \frac{k_B T}{m_e c^2} dl, \quad (2)$$

as well as the kSZ Compton-y in the cluster rest-frame (right panels),

$$y_{kSZ} = \int n_e \sigma_T \frac{v}{c} dl. \quad (3)$$

We compute the kSZ in the rest-frame of the main cluster. In general, the observed kSZ signal will also include a small contribution from the peculiar motion of the cluster itself (Holzapfel et al. 1997; Benson et al. 2003; Hand et al. 2012; Mauskopf et al. 2012; Zemcov et al. 2012). Our simulated cluster has a bulk gas velocity of  $159 \text{ km s}^{-1}$ , consistent with constraints from observations (Planck Collaboration et al. 2013). More importantly, in projection 1 (the projection selected to optimize the kSZ signal from the merging subclusters), the main cluster's bulk line of sight velocity is only  $33 \text{ km s}^{-1}$ , much smaller than the velocities of the merging subclusters (Sections 4.1 and 4.2). For this reason, we do all our analysis in the rest-frame of the main cluster, which does not significantly affect our results, and allows for easy comparison to other simulations as well as observations.

Substructures A and B are both visible as pressure enhancements in the tSZ Compton-y maps shown in Figure 3. The main cluster is clearly unrelaxed and asymmetric, as there are large-scale disturbances in the ICM around both substructures. The kSZ Compton-y map of projection 1 (top right panel of Figure 3) reveals strong and opposing line of sight motions for substructures A and B. We discuss the origins and implications of all these substructures in Section 4. We considered extending the integration depth in each pixel for Equation 2 to  $4 \times R_{200}$ , but because the temperature and density of the gas outside the virial radius is so low, the average Compton-y in each pixel did not change by more than  $\sim 1\%$ .

Observationally, the pixels in Figure 3 are  $10'' \times 10''$  if the cluster is located at a distance corresponding to  $z = 0.32$ , or  $50'' \times 50''$  if the cluster is at distance  $z = 0.05$ . While this sub-arcminute resolution is achievable by current single-dish high-resolution SZE instruments such as MUSTANG (with resolution of  $\sim 10''$ ), the filtering techniques used to remove atmospheric noise in real MUSTANG SZE maps are unable to recover signals on scales larger than  $\sim 45''$ . Interferometric dish arrays have larger spatial dynamic ranges, and arrays such as CARMA are able to probe angular scales of  $\sim 15''$ - $5'$ . While the full angular size of our mock SZE maps may not be possible for large clusters at low redshifts, the results of our investigation are also relevant for mergers occurring closer to the core of the main cluster and SZE-selected clusters at higher redshifts, where angular dynamic range issues are less important. Future instruments and improvements in observational techniques in this emergent field will also be able to increase the angular dynamic range, and so our work also serves as an exploratory proof-of-concept for the science possibilities.

The observable frequency-dependent tSZ spectral distortion of the CMB can be calculated as the change in specific intensity from the Planckian CMB,

$$\Delta I_{tSZ} = I_0 y_{tSZ} \frac{x^4 e^x}{(x^2 - 1)^2} (x \coth\left(\frac{x}{2}\right) - 4) g_{tSZ}(x) \quad (4)$$

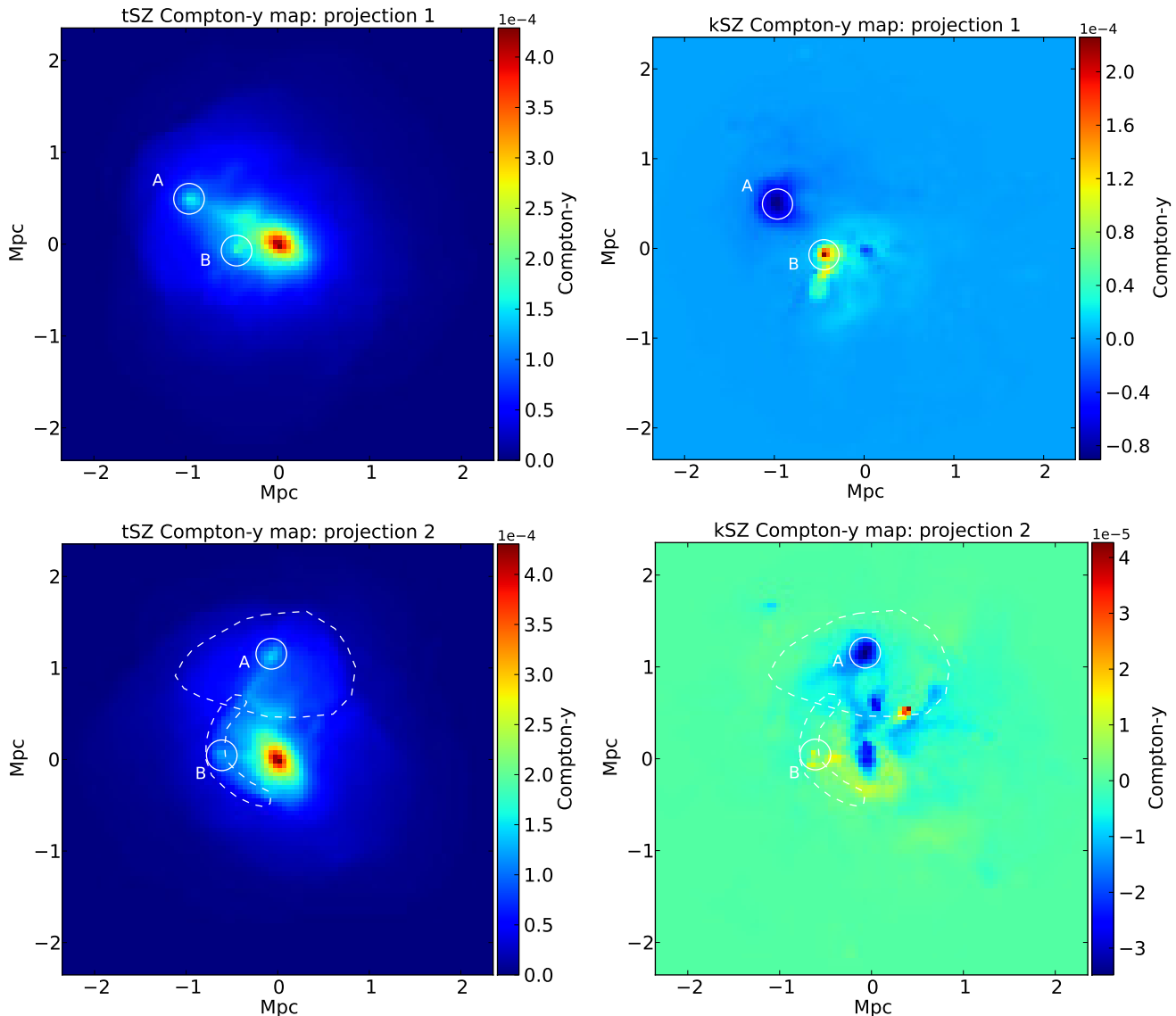


**Figure 3.** Maps of the average Compton- $y$  of the gas along the line of sight of each pixel of the cluster, due to the tSZ (left panels, see Equation 2) and kSZ (right panels, see Equation 3), along projections 1 (top panels) and 2 (bottom panels). Merging substructures A and B are encircled. These two projections are orthogonal, and both substructures have significant (and opposite) line of sight velocities in projection 1, which are transverse velocities in projection 2. The merging substructures are clearly resolved in the kSZ Compton- $y$  map of projection 1 (top right). In the tSZ Compton- $y$  map of projection 2 (bottom left), a bow shock surrounding substructure B (traveling leftwards) and faint extended regions of shocked gas around substructure A (traveling upwards) are visible and encircled with dashed lines. Each pixel is  $50'' \times 50''$  (corresponding to  $47 \text{ kpc} \times 47 \text{ kpc}$ ) if the cluster is at a distance corresponding to a redshift of  $z = 0.05$ .

at dimensionless frequency

$$x = \frac{h\nu}{k_B T}, \quad (5)$$

where  $I_0$  is the specific intensity of the CMB, and  $g_{tSZ}(x)$  are the relativistic corrections calculated in Nozawa, Itoh, & Kohyama (1998). The frequency-dependent spectral distortion due to the kSZ can similarly be calculated using

$$\Delta I_{kSZ} = I_0 y_{kSZ} \frac{x^4 e^x}{(x^2 - 1)^2} g_{kSZ}(x). \quad (6)$$

Figures 4 and 5 shows mock images of the CMB intensity distortion due to the SZE in projections 1 and 2. We chose to generate these mock images at 90 GHz and 268 GHz,

frequencies probed by instruments such as MUSTANG on GBT and Bolocam on CSO, respectively. We also show the kSZ/tSZ intensity distortion fraction in each pixel, and discuss its implications in Section 4.1.

## 4 THE EFFECTS OF MERGERS

### 4.1 SZE Contributions from the kSZ

While most high-resolution SZE observations thus far have been done in a single frequency band, recent progress have been made to image clusters at multiple frequencies by combining observations from different instruments. This

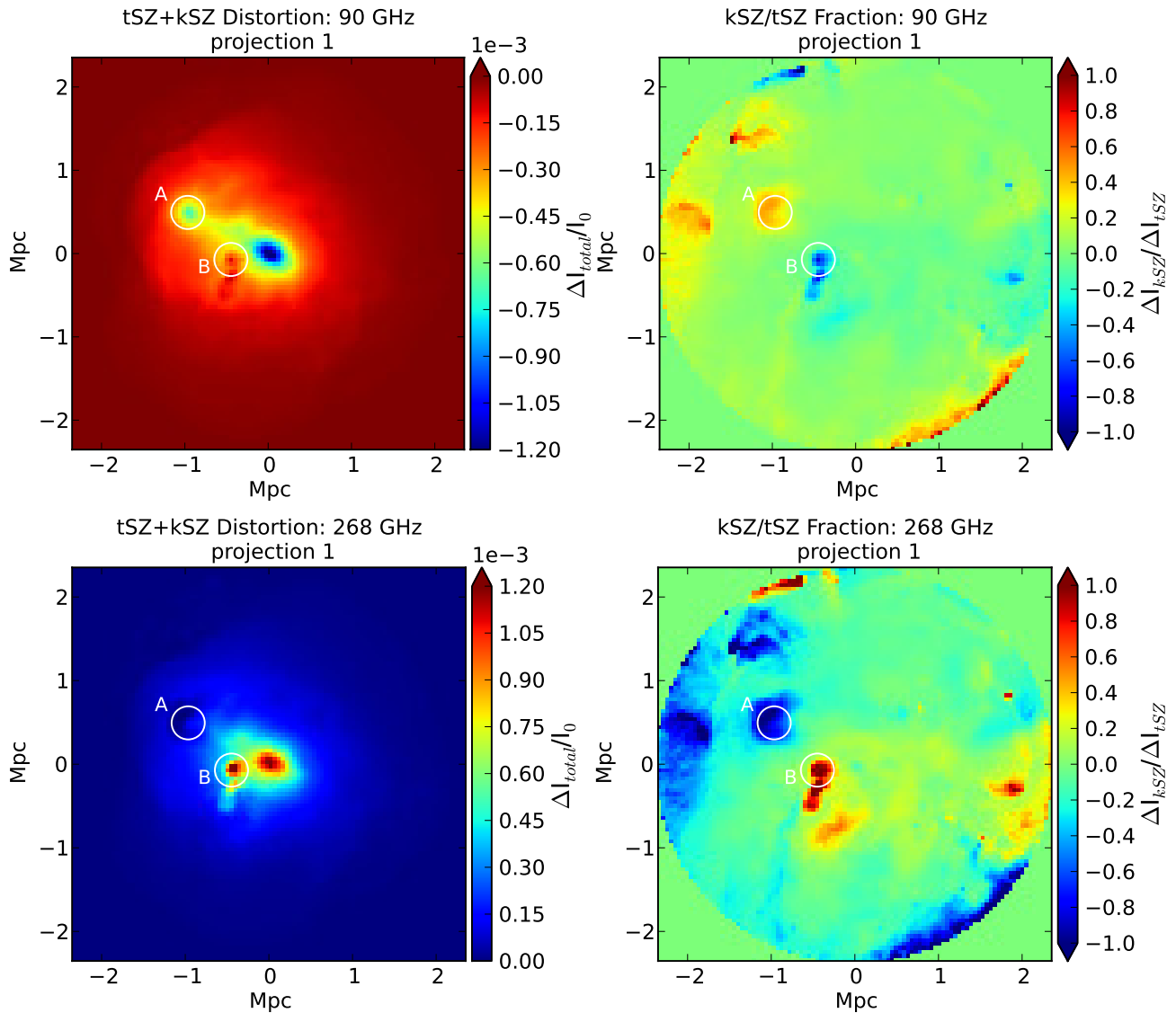


**Figure 4.** Mock images of the total tSZ+kSZ intensity distortion (see Equations 4 and 6) at 90 GHz and 268 GHz in projection 1 (left panels). The appearance and disappearance of substructures A and B at these different frequencies in projection 1 is due to unique frequency-dependence of the kSZ, which can dominate the spectral distortion along merging substructures. Maps of the kSZ/tSZ intensity distortion ratio in these images are also shown (right panels). Large-scale features in these kSZ/tSZ ratio maps not associated with either substructure are due to bulk gas motions in low-density gas, and are not observable in the left panels.

multi-frequency approach is crucial to break the degeneracy between the tSZ and kSZ that exist in single-band observations, by leveraging the unique frequency-dependence of these two effects (see Equations 4 and 6). Recently, Mroczkowski et al. (2012) have shown that significant contributions from the kSZ is necessary to model multi-frequency SZE observations of substructures in a merging system. Based on the inferred kSZ, Mroczkowski et al. (2012) calculated a line of sight velocity of the substructure that is consistent with those determined from optical spectroscopy of the galaxies. Although this is a tantalizing result, these observations carry some uncertainties in the measurement and modeling, as well as the precise origin of the SZE substructure. Using our ability to model the SZE in our cluster simulation and separate the merging substructures from the

ICM, we can investigate the kSZ contribution to the observed SZE and the origins of these observed substructures.

The mock CMB spectral distortion maps of Figures 4 and 5 includes distortion from both the tSZ and kSZ, taking into account their frequency dependence. Projection 1 of our mock SZE maps was selected to highlight the kSZ since in this projection, substructure A has line of sight velocity of  $-1150 \text{ km s}^{-1}$  (away from the observer), while substructure B has line of sight velocity of  $2492 \text{ km s}^{-1}$  (towards the observer) in the rest-frame of the cluster. We see interesting effects in Figure 4 around the substructures when observations at different frequencies are possible. In particular, substructure A appears as a strong CMB intensity decrement at 90 GHz, but is absent in the mock image at 268 GHz. This effect also occurs for substructure B, but in the opposite sense. This can be understood as the effects of the unique

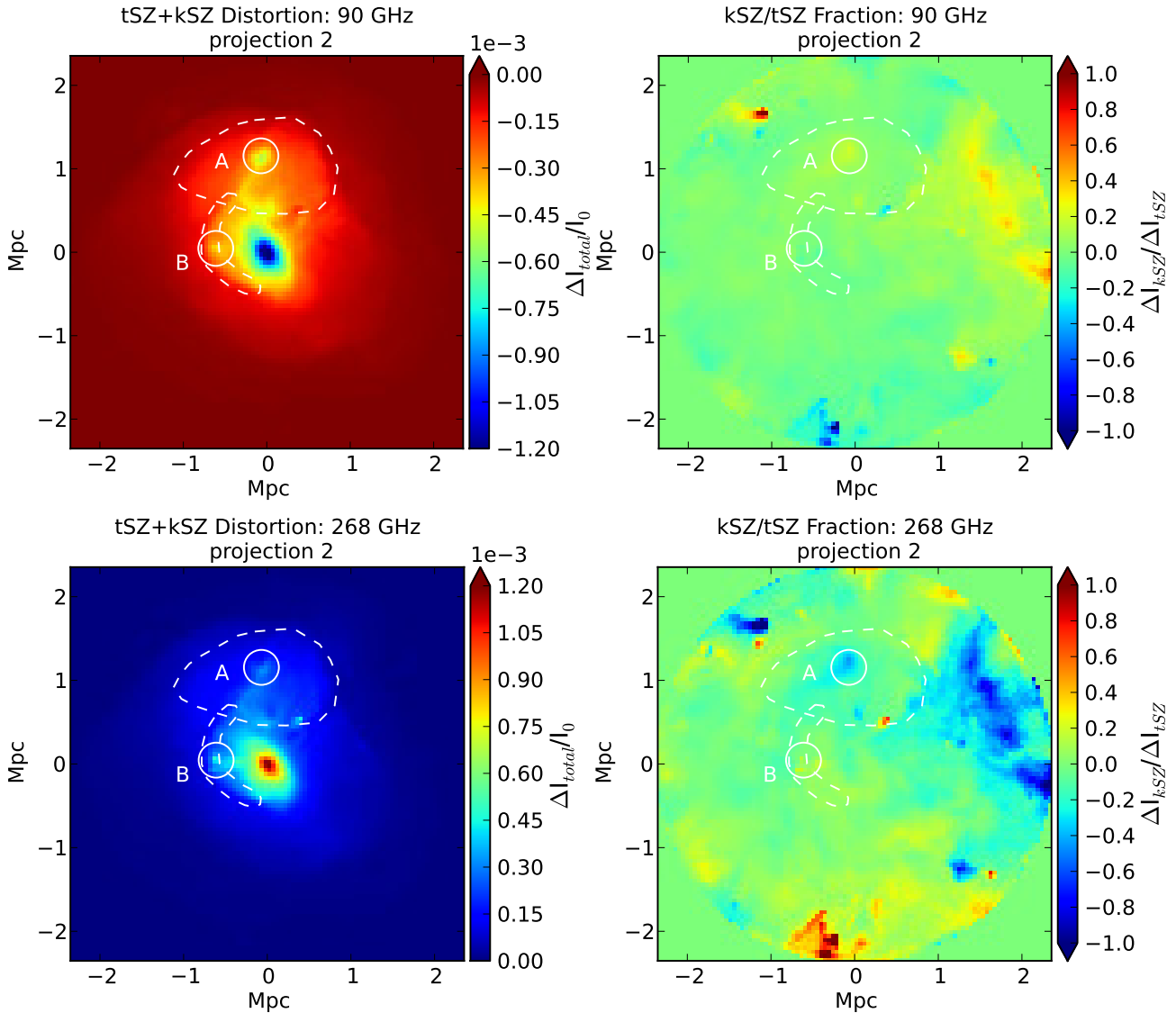


**Figure 5.** Mock images of the total tSZ+kSZ intensity distortion similar to Figure 4, but in projection 2. Shock features, including a bow shock around substructure B (traveling leftwards) and extended regions of shocked gas around substructure A (traveling upwards) are visible and encircled with dashed lines.

frequency-dependence of the tSZ and kSZ, which will cause their relative contributions to the total CMB distortion to vary at different frequencies. These effects are illustrated in Figure 6, which shows the relativistically-corrected CMB spectral distortion for substructures A and B. These spectra have been modeled using gas along the line of sight of the pixel in projection 1 that corresponds to the dense remnant core of each substructure. We can see that for substructure A, its negative line of sight velocity causes a kSZ decrement at 90 GHz, which combines with the negative tSZ decrement at this frequency to produce a large total CMB intensity decrement. At 268 GHz (on the other side of the 217 GHz tSZ null), the tSZ distortion becomes an intensity increment while the kSZ distortion is still a decrement, and so the combination of the two conspires to nullify the SZE distortion. These frequency-dependent effects occur similarly for substructure B, but at opposite frequencies since its positive

line of sight velocity causes the kSZ distortion to become an increment instead at all frequencies.

In Figures 4 and 5 (right panels), we have also shown maps of the kSZ/tSZ CMB intensity distortion fraction. Along the line of sight of substructures A and B in projection 1, the kSZ can contribute significantly to the total SZE distortion, and even dominate over the tSZ. This is extremely important for interpreting high-resolution SZE observations of merging systems, as misinterpretations of the source of SZE substructure may occur if the tSZ-kSZ degeneracy cannot be broken. Single-frequency observations of SZE substructures have often assumed that the kSZ is negligible, which we have shown may not be true in all cases, and so proper interpretation will require multi-frequency observations. Our results showing significant kSZ contributions in merging subclusters should not be surprising, as these effects have already been tentatively observed in Mroczkowski et al. (2012). We note that regions with large kSZ/tSZ CMB

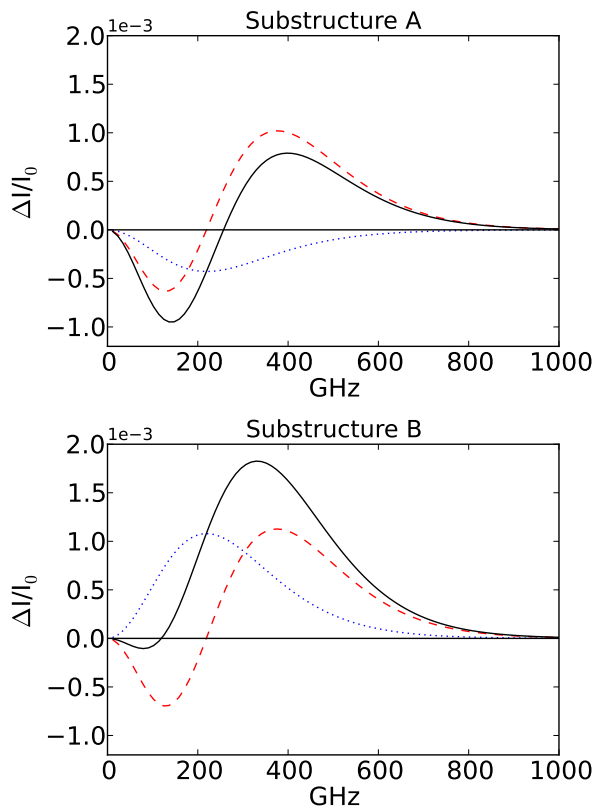


**Figure 6.** Relativistically-corrected CMB spectral distortions of the gas along the line of sight of the remnant cores of substructure A (top) and B (bottom) in projection 1, due to the tSZ (red dashed), kSZ (blue dotted), and the combined t+kSZ distortion (black solid).

intensity distortion fraction in Figures 4 and 5 (right panels) not associated with substructures A and B are bulk motions in the low-density outskirts of the cluster. While these bulk motions may provide additional non-thermal ICM pressure support and affect the integrated Compton-Y, the gas in these regions have low density and are thus not visible in the mock CMB intensity distortion images of Figures 4 and 5 (left panels).

#### 4.2 SZE Substructure from Shocked Gas

SZE substructures in the ICM of several clusters uncovered by recent high-resolution SZE observations have often been attributed to hot, shocked gas associated with mergers (e.g. Korngut et al. 2011; Plagge et al. 2012). In our mock SZE images, projection 2 was selected to highlight the morphology of the merger shock, as both substructures A and B have strong transverse motions in the plane of the images. In the projection 2 view of Figure 5, substructure A is moving approximately upwards with transverse velocity  $1272 \text{ km s}^{-1}$ , and away from the observer with line of sight velocity  $-337 \text{ km s}^{-1}$  in the rest-frame of the cluster. A large region of disturbed gas surrounds substructure A, shocked heated by the merger. This is most clearly visible at 90 GHz (top left panel of Figure 5), and causes the cluster to be asymmetric in these mock images.

In Figure 5, substructure B is moving leftwards with

transverse velocity  $2493 \text{ km s}^{-1}$ , and towards the observer with line of sight velocity  $94 \text{ km s}^{-1}$  in the rest-frame of the cluster. A shock from the merger is visible around substructure B, traveling leftwards. These features are also clearly visible in projected temperature map of the system (not shown). This is reminiscent of the canonical bow shock seen in X-ray observations of the Bullet Cluster, in which the merging subcluster has a similar velocity and mass ratio (Markevitch et al. 2002; Springel & Farrar 2007). The shock front of substructure B is much sharper than that of substructure A because substructure A merged slightly earlier than substructure B. Since substructure A has already traveled into the low-density outskirts of the main cluster at this epoch, its shock front in Figure 5 is much less prominent in high-resolution SZE images than substructure B’s.

#### 4.3 Disentangling Bound Subhaloes from the ICM

Although we have qualitatively described the effects of the kSZ and merger shocks in our mock SZE images, SZE substructures are combinations of a variety of effects and processes. For example, it is unclear whether the strong kSZ along the line of sight of merging substructures discussed in Section 4.1 is due to cold, dense gas in their remnant cores or due to fast moving shocked gas. It would be particularly helpful for interpreting observed SZE substructures to separate the gravitationally-bound subhaloes in our simulated cluster from the background ICM. This will allow us to probe their SZE signals separately and identify the exact origin of the observable SZE substructures. To this end, we run AMIGA Halo Finder (AHF; Gill, Knebe, & Gibson 2004; Knollmann & Knebe 2009) on the main cluster at simulation time step  $z = 0.05$ . AHF recursively identifies density peaks in the cluster in a hierarchical tree at different resolutions to find haloes and their subhaloes (and sub-subhaloes inside subhaloes, etc.), an algorithm well suited for high-resolution cosmological cluster simulations. Once all haloes are isolated, AHF assigns each individual particle to a halo by starting at the smallest haloes and iteratively removing particles in the halo that are gravitationally unbound, assigning them instead to their larger parent halo. The resulting haloes thus consists only of bound particles, robustly separating subhaloes from parent haloes for analysis. This careful separation of bound and unbound particles in each halo is crucial in the dense environments of galaxy clusters, where a significant fraction of gas in the cluster galaxies may not be bound to the galaxy, but are instead part of the background ICM of the main cluster.

From the haloes identified by AHF, substructures A and B are by far the largest subhaloes within the main cluster by more than an order of magnitude, verifying the ability of high-resolution SZE observations to detect large subclusters in clusters. In Figure 7, we produce tSZ and kSZ Compton-y maps of just the background ICM, which is gravitationally bound only to the main cluster and not to any substructures. In other words, we have reproduced Figure 3 after removing all bound substructures. Comparison between Figures 7 and 3 shows that the large high-pressure regions corresponding to substructures A and B are no longer present in the background ICM tSZ Compton-y maps, and instead there are faint cavities since the volume of space occupied by subcluster gas are now empty. The integrated Compton-Y due to

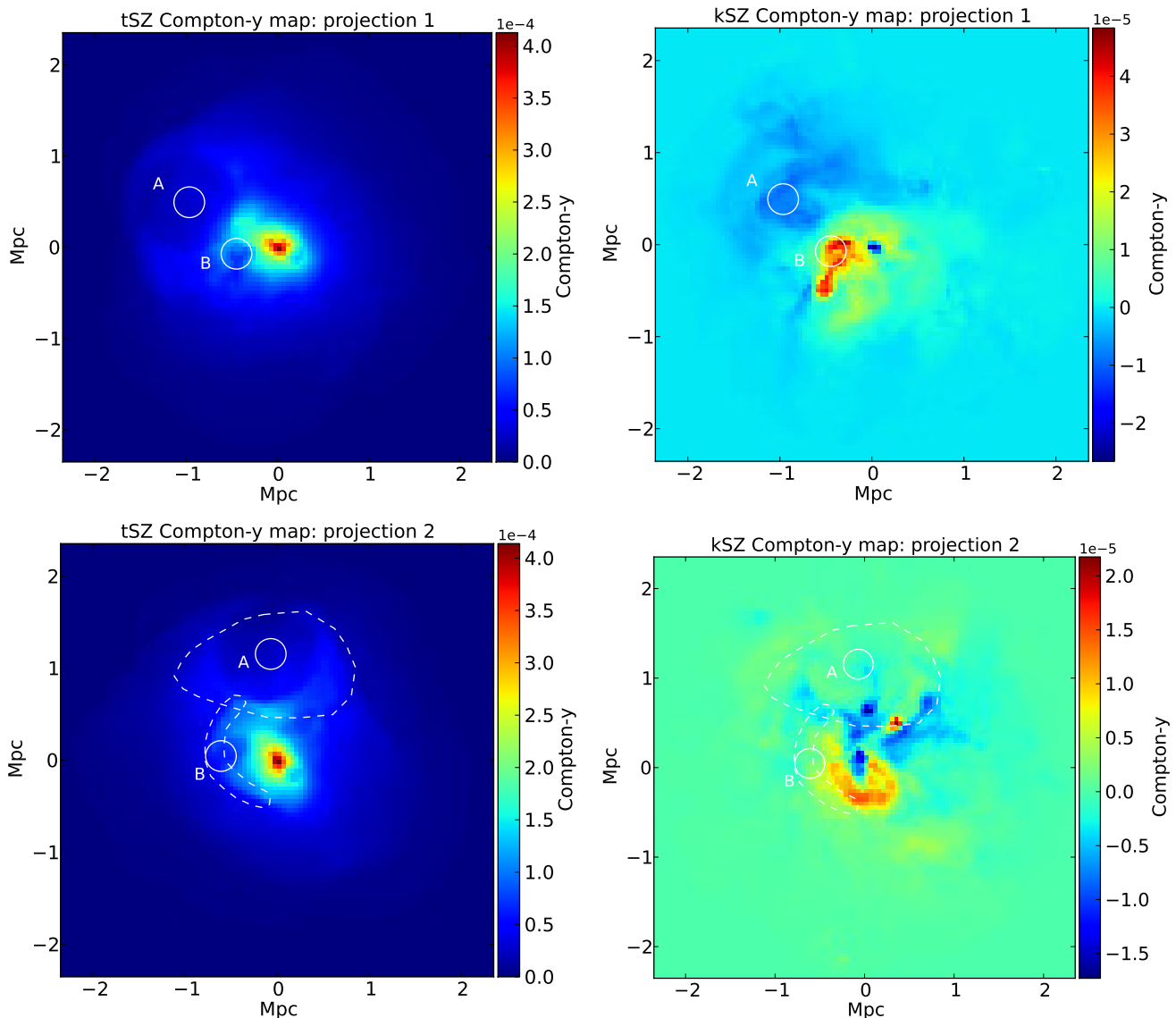


**Figure 7.** Compton- $y$  map of the background ICM, gravitationally bound only to the main cluster and not to any subhaloes, from the tSZ (left column) and kSZ (right column), along projections 1 (top row) and 2 (bottom row). Compared to Figure 3, the kSZ Compton- $y$  around the substructures along projection 1 (top right) are far weaker, while the shocked gas around the substructures in the tSZ Compton- $y$  map along projection 2 (bottom left) are still faintly visible (encircled with dashed lines). This suggests that the observable kSZ is dominated by the gas in the remnant core of the substructures rather than the shock, while shocked gas can produce extended tSZ structures in the background ICM.

the gravitationally-bound gas in substructure A accounts for 10% of the total  $Y_{200}$  of the cluster at this epoch, while substructure B accounts for only 1%. Large-scale disturbances in the background ICM due to shocked gas are still present in the tSZ Compton- $y$  maps, while some line of sight motions in the background ICM around the merging substructures in projection 1 is visible in the kSZ Compton- $y$  maps (especially for substructure B). Mock images of the observable CMB intensity distortions of this background ICM at 90 GHz and 268 GHz are shown in Figures 8 and 9 for projections 1 and 2, respectively. Comparison of Figure 8 to Figure 4 shows that the strong kSZ effects discussed in Section 4.1 originate in the gravitationally-bound gas in the remnant cores, although there is some residual motion in

the background ICM gas induced by the shock (in addition to other turbulent bulk motions), which we discuss in Section 4.4. Comparison of Figure 9 to Figure 5 shows that the bow shock around substructure B and extended regions of shocked gas around substructure A are not gravitationally bound to the subclusters, and have fainter SZE signals than the remnant cores.

#### 4.4 Biases in kSZ Velocity Estimates

Velocity estimates of merging subclusters in high-resolution SZE observations have usually been estimated by first obtaining X-ray temperature and density maps of the main cluster. These X-ray derived values have inherent biases

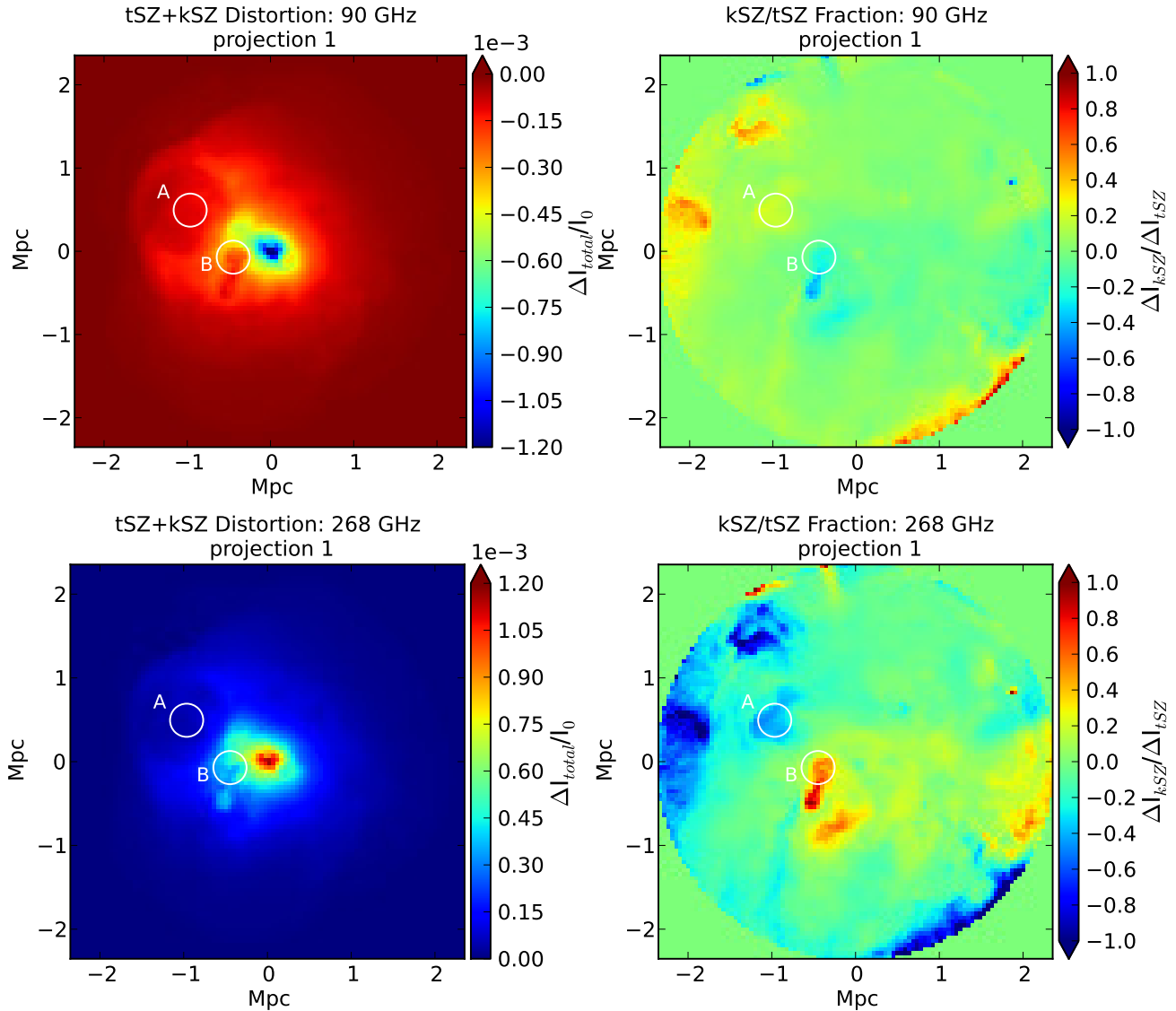


**Figure 8.** Mock images of the total tSZ+kSZ intensity distortion at 90 GHz and 268 GHz, for projection 1 (left column) of the ICM gravitationally bound only to the main cluster and not to any subhaloes (compare to Figure 4). The kSZ/tSZ intensity distortion ratio in each of these maps are also shown (right column).

when compared to SZE observations, including those that stem from the non-trivial differences in the use of X-ray emission-weighted temperatures versus electron density-weighted temperatures (Diaferio et al. 2005), as well as effects of gas clumping. Furthermore, these observations leave temperature fluctuations along the line of sight in each pixel poorly constrained, thus essentially assuming a one-temperature approximation along any particular line of sight. However, assuming that these values are correct, a X-ray derived pseudo-tSZ Compton- $y$  map of the cluster can be calculated and compared to SZE Compton- $y$  maps at different frequencies, assuming all spectral distortions are due to the tSZ (e.g. as done in Mroczkowski et al. 2012). Disagreements between the SZE Compton- $y$  maps and the X-ray pseudo-Compton- $y$  maps will thus likely be due to the kSZ, especially when strongly divergent features on these maps follow the general frequency-dependency of the kSZ (e.g. if the pseudo-Compton- $y$  under-predicts the observed

Compton- $y$  on one side of the tSZ null, and over-predicts on the other). In this way, the kSZ substructures can be identified, and the spectral distortion region surrounding these kSZ substructures can be fitted with a tSZ+kSZ model to determine the line of sight velocity of the merging subcluster.

Similar to the one-temperature approximation, estimation of the subcluster line of sight velocity using the above method also assumes that the gas along the line of sight of the merging subcluster has one velocity. Of course, not all the gas along that line of sight has the same velocity as the subcluster. The background ICM is well-known to have large-scale turbulent bulk motions, but these gas motions will have random directions, and usually smaller velocities. Contribution of the motions of the background ICM to the kSZ along the line of sight of merging subclusters may thus bias kSZ-based subcluster velocity estimates in high-resolution observations in ways that are currently unclear.

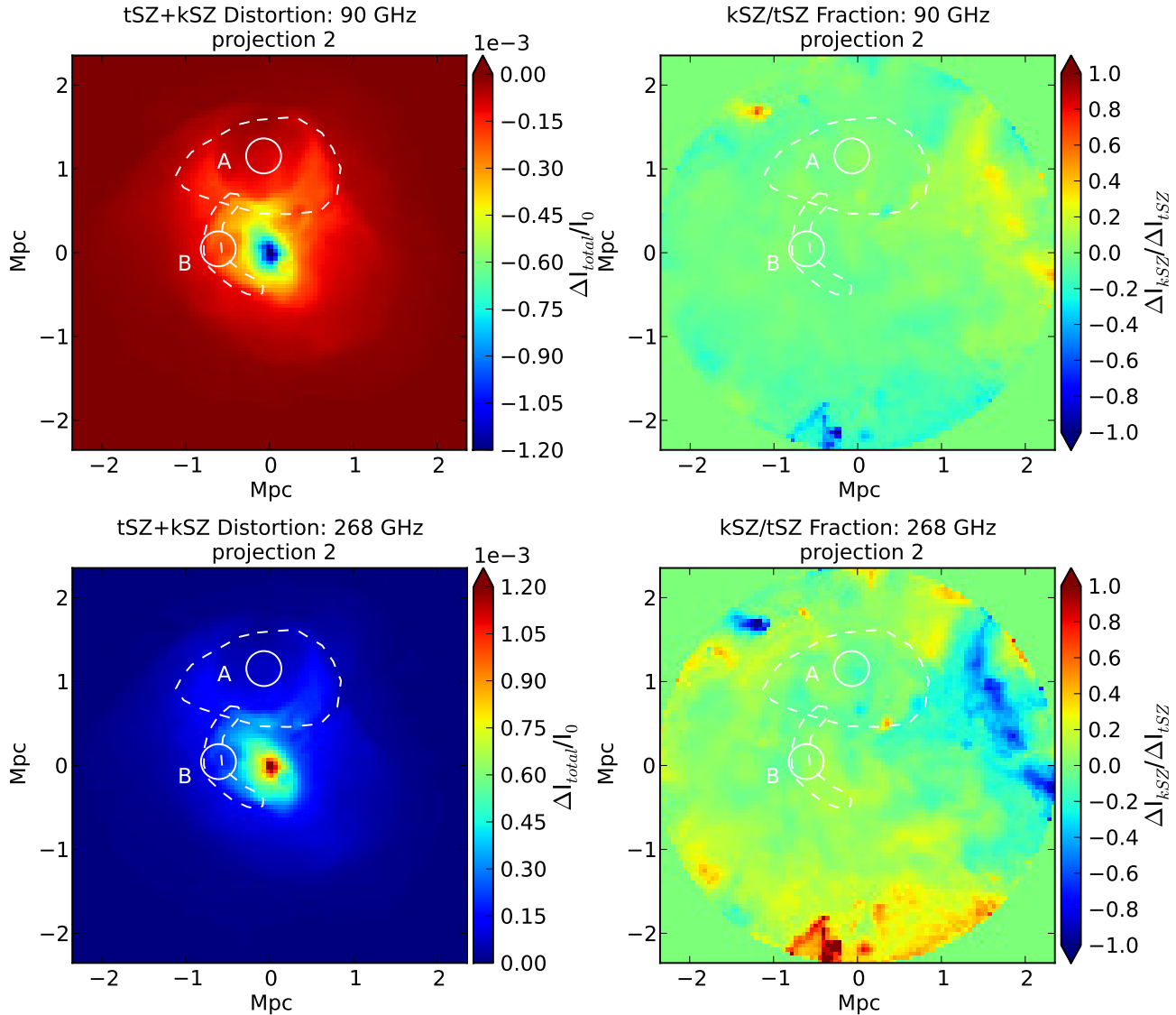


**Figure 9.** Mock images of the total tSZ+kSZ intensity distortion for the ICM gravitationally bound only to the main cluster, similar to Figure 8 but for projection 2 (compare to Figure 5).

To probe this bias using a simulation requires comparing the mass-weighted velocity along the line of merging subclusters to their true velocity as determined by isolating the subclusters using a halo-finder.

Using the gas particles in substructures A and B identified and isolated by AHF, we calculate their true particle mass-weighted velocities in the pixels along the centers of their remnant cores in projection 1 of Figure 3. We then compare this true velocity of the subclusters to the particle mass-weighted velocity inferred from the kSZ distortion in Figure 6, which essentially adds the kSZ contribution from motions in the background ICM gas along the pixel in the calculation. We find that for substructure A, the line of sight velocity estimate including the background ICM is only 4% smaller than the true line of sight velocity, while for substructure B it is 12%. Thus, the bias in the estimated velocity due to the background ICM is on the order of  $\sim 10\%$  in our simulated cluster. The underestimate of the velocity

is larger for substructure B due to its closer line of sight position to the core of the main cluster in projection 1, and so the denser ambient ICM along its line of sight affects its velocity estimates more significantly.

The small magnitude of biases in the velocity estimates for both subclusters is primarily due to the large density of the subcluster remnant cores in comparison to the much lower density of the background ICM (see discussion in Section 4.3). This causes the kSZ along the line of sight of the subclusters to be dominated by the motion of the dense gravitationally-bound gas in the merging subcluster, and so the resulting velocity estimation is fairly accurate. However, an important secondary factor is the additional contributions to the kSZ along the line of sight of the subclusters from bulk gas motion in the background ICM induced by the merger. The gas in the background ICM with bulk motion includes merger-shocked gas, as well as gas stripped away from the merging subcluster due to ram-pressure stripping.

Although the kSZ signal from this motion in the background ICM is relatively minor (e.g. the kSZ Compton- $y$  is relatively small around the merging subclusters in the top right panel of Figure 7 in comparison to the same region in Figure 3), the background ICM gas along the line of sight will have velocity vectors in the same direction as the merging subclusters. Thus, the background ICM gas will contribute some non-zero kSZ signal that is preferentially in the same direction as the merging subcluster, reducing the bias on the inferred velocity of the subcluster.

To gauge the effect of the bulk gas motions on our kSZ-inferred substructure velocities, we recalculate the kSZ-inferred velocities assuming that the background gas not in the merging substructures (but along the line of sight of their remnant cores) have zero velocity, effectively removing any kSZ signal from the background ICM. Although this may seem unrealistic since the background ICM is known to have turbulent bulk motions, these motions not induced by the merger will have random velocity vectors, and do not substantially contribute to the kSZ Compton- $y$ . In this extreme limit of a motionless background ICM, the line of sight velocity estimates for substructures A and B are underestimated by 13% and 25%, respectively. Thus, the motion of the background ICM gas induced by the merger reduces the bias on the velocity estimate by a factor of  $\sim 2$  to 3. This is a promising result for high-resolution SZE observations, and shows that the bias in the one-velocity approximation along the line of sight of merging subcluster due to the background ICM is not dominant in comparison to other sources of bias in observations.

## 5 SUMMARY AND CONCLUSIONS

Using a high-resolution zoomed-in cosmological simulation of a galaxy cluster, we model the tSZ and kSZ CMB spectral distortion to investigate the observable substructures during a 10:3:1 ratio triple merger. We create mock SZE images of the merging cluster at the peak of its integrated Compton- $Y$ , where substructures are likely to be most prominent and the cluster is most detectable in blind SZE surveys. Our mock images are produced in two perpendicular projections, the first to highlight the effects of the kSZ, and the second to highlight the effects of merger shocks on the background ICM. The two merging subclusters are clearly observable in our mock SZE images, with opposing velocities in the main cluster rest-frame. Using the AMIGA Halo Finder, we separate the two gravitationally-bound merging substructures from the main cluster to investigate the relative contributions of the substructure and main cluster ICM gas to the observable SZE in high-resolution observations. In particular, we find the following.

(1) SZE spectral distortions along the line of sight of merging subclusters can be dominated by the kSZ if the subclusters' line of sight velocities are large. Single-frequency observations leaving the kSZ unconstrained may lead to misinterpretations. Multi-frequency observations that take advantage of the unique frequency-dependence of the tSZ and kSZ are key to studying merging systems.

(2) The remnant cores of merging subclusters are visible in resolved SZE images, and in the triple merger of our simu-

lated cluster, they contribute 10% and 1% to the integrated Compton- $Y$ .

(3) Merger shock features including shock fronts, extended regions of shock-heated gas, and strong asymmetry of the cluster due to large disturbed regions can be visible in high-resolution SZE images. Future follow-up of SZE-selected clusters will be helpful to identify merging and disturbed clusters, important for reducing scatter in cluster scaling relations induced by these systems.

(4) kSZ velocity estimates of merging subclusters using a one-velocity approximation for all gas along the line of sight of the subclusters (including the background ICM) is generally accurate to  $\sim 10\%$  in our simulated cluster. This accuracy is primarily due to the dominance of the kSZ along the line of sight by the dense remnant core of the merging subcluster, but an important secondary factor is the kSZ contribution from bulk motions in the background ICM induced by the merger. Since the merger shock and ram-pressure stripped gas will cause bulk motions in the background ICM along the line of sight in the same direction as the merging subclusters, it will reduce the velocity bias in the one-velocity approximation by a factor of  $\sim 2$ -3.

Current high-resolution SZE observations have already begun to uncover substructures associated with mergers in clusters, and have detected strong kSZ contributions from motions of merging subclusters. Our encouraging results indicate that these types of SZE observations at multiple frequencies can robustly probe both the thermal and dynamic state of the ICM. Next-generation high-resolution SZE instruments such as MUSTANG-2 and ALMA's band 1 will also be able to quickly survey large numbers of clusters with much higher sensitivities on a variety of angular scales and resolutions. Aside from their important impact on cluster cosmology, these observations could also be interesting probes of other phenomena in the ICM, such as those in the central regions of cool core clusters. The ability to separate the tSZ and kSZ distortions may allow investigation of the coupling of the central AGN to the surrounding ICM, where AGN heating of the cooling core gas could be thermal and/or kinetic in nature. Our results offer only a glimpse of the science possibilities with high-resolution SZE observations, and further simulations including more baryon physics to complement these observations will be necessary.

## 6 ACKNOWLEDGMENTS

The authors wish to thank Sarah R. Loebman for help with using AMIGA-AHF, and the anonymous referee for a very thorough review of this paper. JJR and TRQ acknowledge support from the NSF AISRP program for development of the simulation analysis software, and NSF PHY-0205413 for ChaNGa development. Resources supporting this work were provided by the NASA High-End Computing (HEC) Program through the NASA Advanced Supercomputing (NAS) Division at Ames Research Center. The authors also acknowledge the Texas Advanced Computing Center (TACC) at The University of Texas at Austin for providing HPC resources that have contributed to the research results reported within this paper, as well as computing resources provided by WestGrid and Compute/Calcul Canada.

**REFERENCES**

- Allen S. W., Evrard A. E., Mantz A. B., 2011, *ARA&A*, 49, 409
- Arnaud M., Pratt G. W., Piffaretti R., Böhringer H., Croston J. H., Pointecouteau E., 2010, *A&A*, 517, A92
- Battaglia N., Bond J. R., Pfrommer C., Sievers J. L., 2012, *ApJ*, 758, 74
- Benson B. A., et al., 2003, *ApJ*, 592, 674
- Birkinshaw M., 1999, *PhR*, 310, 97
- Bock D. C.-J., et al., 2006, *SPIE*, 6267,
- Carlstrom J. E., Holder G. P., Reese E. D., 2002, *ARA&A*, 40, 643
- Carlstrom J. E., et al., 2011, *PASP*, 123, 568
- Diaferio A., et al., 2005, *MNRAS*, 356, 1477
- Dicker S. R., et al., 2008, *SPIE*, 7020,
- Fowler J. W., et al., 2007, *ApOpt*, 46, 3444
- Gioachin, F., Sharma, A., Chakravorty, S., Mendes, C., et al., 2007, in M. Dayd et al., eds, *High Performance Computing for Computational Science - VECPAR 2006*, 476
- Gill S. P. D., Knebe A., Gibson B. K., 2004, *MNRAS*, 351, 399
- Haig D. J., et al., 2004, *SPIE*, 5498, 78
- Hand N., et al., 2012, *PhRvL*, 109, 041101
- Hoekstra H., Mahdavi A., Babul A., Bildfell C., 2012, *MNRAS*, 427, 1298
- Holzappel W. L., Ade P. A. R., Church S. E., Mauskopf P. D., Rephaeli Y., Wilbanks T. M., Lange A. E., 1997, *ApJ*, 481, 35
- Katz N., White S. D. M., 1993, *ApJ*, 412, 455
- Kitayama T., Komatsu E., Ota N., Kuwabara T., Suto Y., Yoshikawa K., Hattori M., Matsuo H., 2004, *PASJ*, 56, 17
- Knollmann S. R., Knebe A., 2009, *ApJS*, 182, 608
- Komatsu E., et al., 2009, *ApJS*, 180, 330
- Korngut P. M., et al., 2011, *ApJ*, 734, 10
- Krause E., Pierpaoli E., Dolag K., Borgani S., 2012, *MNRAS*, 419, 1766
- Kravtsov A. V., Borgani S., 2012, *ARA&A*, 50, 353
- Lau E. T., Kravtsov A. V., Nagai D., 2009, *ApJ*, 705, 1129
- Mantz A., Allen S. W., Ebeling H., Rapetti D., 2008, *MNRAS*, 387, 1179
- Mantz A., Allen S. W., Rapetti D., Ebeling H., 2010, *MNRAS*, 406, 1759
- Marrone D. P., et al., 2012, *ApJ*, 754, 119
- Markevitch M., Gonzalez A. H., David L., Vikhlinin A., Murray S., Forman W., Jones C., Tucker W., 2002, *ApJ*, 567, L27
- Mason B. S., et al., 2010, *ApJ*, 716, 739
- Maturi M., Moscardini L., Mazzotta P., Dolag K., Tormen G., 2007, *A&A*, 475, 71
- Mauskopf P. D., et al., 2012, *MNRAS*, 421, 224
- Mroczkowski T., et al., 2012, *ApJ*, 761, 47
- Nord M., et al., 2009, *A&A*, 506, 623
- Nozawa S., Itoh N., Kohyama Y., 1998, *ApJ*, 508, 17
- Plagge T. J., et al., 2012, *arXiv*, arXiv:1203.2175
- Planck Collaboration, et al., 2011a, *A&A*, 536, A1
- Planck Collaboration, et al., 2011b, *A&A*, 536, A9
- Planck Collaboration, et al., 2012a, *arXiv*, arXiv:1208.3611
- Planck Collaboration, et al., 2012b, *arXiv*, arXiv:1204.2743
- Planck Collaboration, et al., 2012c, *A&A*, 543, A102
- Planck Collaboration, et al., 2013, *arXiv*, arXiv:1303.5090
- Poole G. B., Babul A., McCarthy I. G., Fardal M. A., Bildfell C. J., Quinn T., Mahdavi A., 2007, *MNRAS*, 380, 437
- Randall S. W., Sarazin C. L., Ricker P. M., 2002, *ApJ*, 577, 579
- Reese E. D., et al., 2012, *ApJ*, 751, 12
- Roncirelli M., Moscardini L., Borgani S., Dolag K., 2007, *MNRAS*, 378, 1259
- Rozo E., et al., 2010, *ApJ*, 708, 645
- Sehgal N., et al., 2011, *ApJ*, 732, 44
- Seljak U., Zaldarriaga M., 1996, *ApJ*, 469, 437
- Semoloni F., Yepes G., De Petris M., Gottlöber S., Lamagna L., Comis B., 2013, *MNRAS*, 429, 323
- Sifon C., et al., 2012, *arXiv*, arXiv:1201.0991
- Springel V., Farrar G. R., 2007, *MNRAS*, 380, 911
- Sunyaev R. A., Zeldovich Y. B., 1970, *CoASP*, 2, 66
- Sunyaev R. A., Zeldovich Y. B., 1972, *CoASP*, 4, 173
- Vanderlinde K., et al., 2010, *ApJ*, 722, 1180
- Vikhlinin A., et al., 2009, *ApJ*, 692, 1060
- Wik D. R., Sarazin C. L., Ricker P. M., Randall S. W., 2008, *ApJ*, 680, 17
- Zeldovich Y. B., Sunyaev R. A., 1969, *Ap&SS*, 4, 301
- Zemcov M., et al., 2012, *ApJ*, 749, 114